Heliyon 7 (2021) e08207

Contents lists available at ScienceDirect

Heliyon

journal homepage: www.cell.com/heliyon

Research article

Modeling viral dynamics in SARS-CoV-2 infection based on differential equations and numerical analysis

Mitsuhiro Odaka [a,b,*], Katsumi Inoue [b,a]

[a] Department of Informatics, The Graduate University for Advanced Studies, SOKENDAI, 2-1-2 Hitotsubashi, Chiyoda-ku, Tokyo, 101-8430, Japan
[b] Principles of Informatics Research Division, National Institute of Informatics, 2-1-2 Hitotsubashi, Chiyoda-ku, Tokyo, 101-8430, Japan

ARTICLE INFO

Keywords:
SARS-CoV-2
COVID-19
Computer simulation
Virus replication
Computational biology
Host-pathogen interactions
Virus shedding
Viral load
Nonlinear dynamics
Cell count

ABSTRACT

Computational modeling and simulation of viral dynamics would explain the pathogenesis for any virus. Such computational attempts have been successfully made to predict and control HIV-1 or hepatitis B virus. However, the dynamics for SARS-CoV-2 has not been adequately investigated. The purpose of this research is to propose different SARS-CoV-2 dynamics models based on differential equations and numerical analysis towards distilling the models to explain the mechanism of SARS-CoV-2 pathogenesis. The proposed four models formalize the dynamical system of SARS-CoV-2 infection, which consists of host cells and viral particles. These models undergo numerical analysis, including sensitivity analysis and stability analysis. Based on the sensitivity indices of the four models' parameters, the four models are simplified into two models. In advance of the following calibration experiments, the eigenvalues of the Jacobian matrices of these two models are calculated, thereby guaranteeing that any solutions are stable. Then, the calibration experiments fit the simulated data sequences of the two models to two observed data sequences, SARS-CoV-2 viral load in mild cases and that in severe cases. Comparing the estimated parameters in mild cases and severe cases indicates that cell-to-cell transmission would significantly correlate to the COVID-19 severity. These experiments for modeling and simulation provide plausible computational models for the SARS-CoV-2 dynamics, leading to further investigation for identifying the essential factors in severe cases.

1. Introduction

Coronavirus disease 2019 (COVID-19) is an infectious disease caused by severe acute respiratory syndrome coronavirus 2 (SARS-CoV-2) [1]. SARS-CoV-2 infects bronchial epithelial cells, pneumocytes, or alveolar macrophages and causes severe symptoms such as acute respiratory distress syndrome (ARDS) due to excessive production of inflammatory cytokines known as a cytokine storm [2]. The first death in Wuhan City in January 2020 and the cumulative number of deaths worldwide, approximately four million in July 2021, have been confirmed [3]. Under this situation, the attempts to address the COVID-19 pandemic have been promoted for uncovering the principle of SARS-CoV-2 pathogenesis. Notable one of these attempts is computational modeling and simulation of transmission dynamics. Modeling and simulation studies of transmission dynamics *between individuals* for any pathogen have originated mathematical epidemiology more than a century before [4]. For example, Hamer built a transmission dynamics model of measles in 1906 [5], and Ross presented a model of malaria in 1911 [6]. Kermack and McKendrick *et al.* established mathematical theory for epidemics around the 1930s [7, 8]. These computational models have influenced the development of the various models describing the SARS-CoV-2 transmission dynamics between individuals [9, 10]. Nevertheless, the underlying mechanism of SARS-CoV-2 pathogenesis has not been understood because modeling of the SARS-CoV-2 transmission dynamics *within individuals* is not investigated enough to reproduce *in vivo* data on COVID-19. Namely, plausible and straightforward models have been required for explaining the mechanism of SARS-CoV-2 pathogenesis. Therefore, exploring and comparing different SARS-CoV-2 dynamics models should provide a novel envision of the dynamical system's behavior within the COVID-19 patients. The endeavors to quantify *in vivo* temporal change of cellular population or virulence within individuals have originated the isolation of the Human Immunodeficiency Virus (HIV) in 1983 [11]. Modeling techniques concerning transmission dynamics between individuals met this HIV isolation, forming a significant starting point for advances in the studies on *viral dynamics*, transmission dynamics within individuals based

* Corresponding author at: Department of Informatics, The Graduate University for Advanced Studies, SOKENDAI, 2-1-2 Hitotsubashi, Chiyoda-ku, Tokyo, 101-8430, Japan.
E-mail address: odaka@nii.ac.jp (M. Odaka).

https://doi.org/10.1016/j.heliyon.2021.e08207

on computational modeling and simulation with time-series clinical or experimental data [12]. The first baseline viral dynamics model with ordinary differential equations (ODEs) was the HIV-1 dynamics model introduced by Perelson in 1996 [13]. This Perelson's model has described experimental or clinical data on HIV-1 or hepatitis B virus and quantified the virulence at the cellular scale, including viral burst size, basic reproduction number, and viral particle copies' or cells' mean lifetime [14, 15]. Based on the Perelson's model, varied viral dynamics models have been constructed, including a model of macrophage with immune cell influx in inflammation [16], a model of neural progenitor cells' dynamics in neurogenesis [17], or a model with mixed infection [18]. Moreover, the viral dynamics models have succeeded in predicting intervention outcomes or planning practical experiments [19]. The purpose of this paper includes the following two things: first, to build and compare multiple SARS-CoV-2 dynamics models based on ODEs; second, to fit the models to two cases of the observed COVID-19 experimental data. Compared to the existing research, the foci of this paper are on constructing different SARS-CoV-2 dynamics models by abstracting *in vivo* SARS-CoV-2 pathogenesis as dynamical systems and distilling beneficial models that describe the population dynamics of host cells and viral particles. On building the SARS-CoV-2 dynamics models, numerical analysis enhances the quality of modeling and simulation. In particular, pruning the fixable parameters based on sensitivity indices simplifies the redundant models, thereby balancing the model complexity and simplicity. Calculating the eigenvalues of the simplified models guarantees the solutions' orbital stability. Further, the calibration experiments fit the simulated data generated from the models to two cases of actual observed data. Here, the comparison of the parameter values estimated from the viral load data sequence in mild patients and those in severe cases clarifies the relationship between the key parameters and the COVID-19 severity. This paper is an extension of the previous work, which has contributed to computational modeling and computer simulation of SARS-CoV-2 viral load kinetics and suggested a qualitative relationship between the asymptomatic carriers' reactivation risk and the COVID-19 severity [20]. As an improvement of the previous work, this paper introduces different models, extends the scope of sensitivity analysis from one model to four models to simplify the models, evaluates the equilibrium solution's stability to ensure stable calibration, and conducts the calibration experiments to avoid local minima. The rest of the paper is organized as follows: Section 2 introduces four viral dynamics models. Section 3 explains the methods for data preparation, sensitivity analysis, stability analysis, and calibration experiments. Section 4 shows the results and expands the discussion. Section 5 is devoted to providing related work. Section 6 concludes with a summary of contributions, limitations, and future work.

2. Proposed models

This section formalizes the SARS-CoV-2 dynamical system consisting of host cells and viral particles with four computational models. The first three of four have successfully explained viral dynamics on other viruses, whereas the appropriate investigation of these models for SARS-CoV-2 dynamics has not been conducted. The last one is a newly constructed model.

2.1. Perelson's model (baseline)

Perelson's model mentioned in the previous section has described the time course of three time-dependent state variables called T, I, and V. These state variables $(T, I, V)^{\mathrm{T}} \in \mathbb{R}^3$ correspond to the host's target cell density (susceptible cell count), the host's infectious cell density, and viral quantification measure density, respectively. Here, the dynamical system is assumed as a homogeneous well-stirred reaction system, independent of spatial distribution within each compartment. The state transition diagrams of a single target cell, a single infectious cell, and a viral particle per unit time are illustrated in Fig. 1.

A single target cell becomes infectious proportionally to viral particles density V. Let β be the proportionality constant involved in this infection establishment (virus infection rate). A single target cell turns into an infectious cell at a rate of βV. A single target cell also dies at a rate of μ_1 (target cell mortality). A single infectious cell is removed at a rate of μ_2 (infectious cell mortality) due to activated cell death or cell degeneration associated with virus replication or cytotoxicity during the immune response. A single viral particle is removed at a rate of μ_3 (virus mortality) by the culture medium exchange or physiological reaction or antibody neutralization reaction. Summing up the population of target cells, infected cells, and viral particles whose state transitions are described above for any individual, viral dynamics is regarded as population dynamics. Additionally, infectious cells replicate, release and replenish new viral particles to V in proportion to I. Let k be this proportionality constant (viral shedding rate). Therefore, the ODEs of the baseline viral dynamics model are as follows:

$$\frac{dT}{dt} = -\beta TV - \mu_1 T,$$
$$\frac{dI}{dt} = \beta TV - \mu_2 I,$$
$$\frac{dV}{dt} = -\mu_3 V + kI.$$

2.2. Huang's model (functional response)

While Perelson's baseline model has demonstrated virus replication or host-pathogen interactions well, some experts have regarded it as a too simple model due to its linear infection rate β. Huang *et al.* expressed a more realistic infection rate bound to overhead by introducing a nonlinear term (*functional response*) [21]. By introducing the functional response, the shape of a rectangular hyperbola indicates the actual incidence rate well. This nonlinear term is $\beta TV/(1 + aT + bV)$, where a and b are constant values greater than or equal to zero. The term is similar to the Holling type II incidence functional response. Still, the additional term bV representing a mutual interference between viruses makes it different from Holling type II [22, 23].

2.3. Pearce-Pratt-Phillips model (viral synapse)

While the above models have taken a single transmission chance into account, in 1994, Pearce-Pratt and Phillips *et al.* explicitly presented a scheme of HIV transmission via two routes: cell-free transmission and cell-to-cell transmission [24]. Specifically, the structure mediating the cell-to-cell transmission as a counterpart of the cell-free transmission is called *viral synapse* [25]. Given that both SARS-CoV-2 and HIV have the spike glycoprotein on the surface of the viral envelope [26] and that it has a similar function such as viral entry, receptor recognition, cell attachment, and fusion [27], the viral synapse is presumably in the SARS-CoV-2 life cycle as well. Fig. 2 shows a schematic representation of the SARS-CoV-2 life cycle to explain the differences in two types of transmissions and wherein the viral shedding constant k is also relevant.

A free viral particle attaches to a target cell binding to angiotensin-converting enzyme 2 (ACE2) receptor on the cell membrane supported by spike protein degradation by transmembrane protease serine 2 (TMPRSS2) [28, 29]. Without elaborating on the detailed translation process to replication, the copied viral particles are released at the magnitude of k. The cell-free transmission involves these multiplied viral particles' attachment to other cells after shedding to the extracellular matrix [30]. Consequently, the degree of cell-free transmission is proportional to the viral particle density. β_1 denotes this proportionality constant.

During the cell-to-cell transmission, viral particles directly enter neighboring cells through viral synapse mediated by cellular adhesion molecules [31]. Thus, the level of this direct entry is supposed to be proportional to the infectious cell density. β_2 is set as this proportionality constant. Reflecting the two transmission types, one obtains a term for infection rate as $\beta_1 TV + \beta_2 TI$.

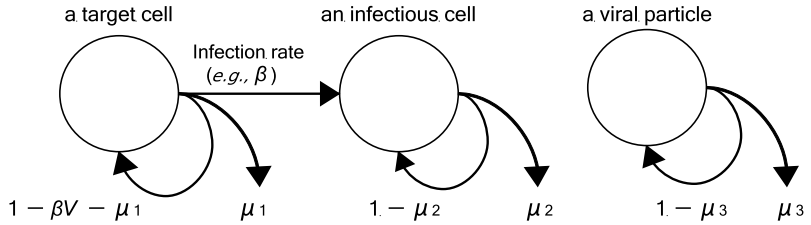

Fig. 1. State transition diagrams of viral dynamics model. The diagrams illustrate three states, including a target (susceptible) cell, an infectious cell, and a viral particle, and their transitions. A single target cell turns into an infectious cell at an infection rate β proportional to viral particles density V. These are dead or killed at each mortality rate μ_1, μ_2, and μ_3.

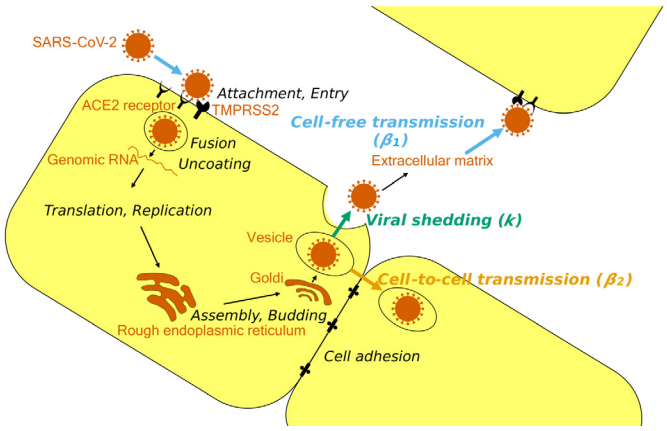

Fig. 2. Schematic representation of severe acute respiratory syndrome coronavirus 2 (SARS-CoV-2) life cycle. Here we assume the unknown direct viral transfer, cell-to-cell transmission (highlighted dense yellow), to be included in the SARS-CoV-2 life cycle, contrasting indirect viral transfer, cell-free transmission (highlighted skyblue). A particle of SARS-CoV-2 infects a host cell at a cell-free transmission rate β_1, binding to angiotensin-converting enzyme 2 (ACE2) receptor helped by transmembrane protease serine 2 (TMPRSS2). The virus undergoes the subsequent typical processes, finally being released (highlighted green) at a viral shedding rate k. Here, the virus in the host cell infects another cell at a cell-to-cell transmission rate β_2. The rest of colors are as follows: black-colored texts and arrows are life-cycle processes; black-colored borders are cellular/vesicular membranes and membrane proteins; orange-colored texts and objectives are viruses, organelles, and extracellular matrix.

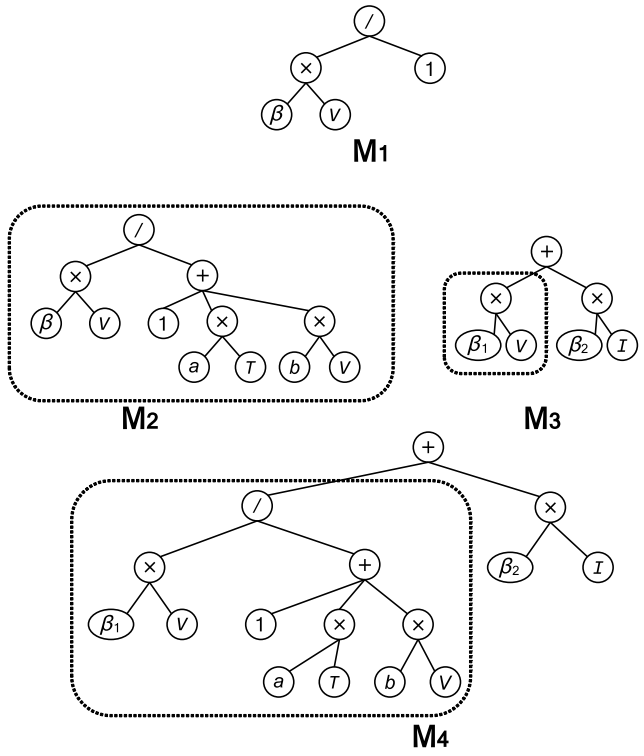

Fig. 3. Infection rate terms of viral dynamics models. The parse trees stand for the infection rate terms of different viral dynamics models; M_1, M_2, M_3, and M_4. The trees consist of arithmetic operators and the variables and constants in Table 2. The trees of Huang's model M_2 and Pearce-Pratt-Phillips model M_3 originate from that of the baseline model M_1. The dashed subtree mutation between M_2 and M_3 generates the tree of an original model M_4.

2.4. New model (functional response and viral synapse)

The models reviewed above could have caused one to have a bias in exploring models due to one's subjective point of view [32]. Procedurally generating a model outside the scope of subjective bias compensated for the above models [33]. For simplicity, M_1, M_2, M_3 denote the above models in short. The machinery manipulation of subtree mutation of M_2 and M_3 generated a new model M_4. Fig. 3 shows the parse trees reflecting the infection rate terms of M_1, M_2, M_3, and M_4. Substituting the dashed subtree of M_3 with the dashed subtree of M_2 generated the parse tree for the infection rate term of M_4.

This section has prepared the four models with different terms for the infection rate. Table 1 is a summary of the difference among the models. Table 2 is a summary of the symbols, definitions, and ranges of the variables and constants of the ODEs.

3. Proposed methods

This section covers data and the remaining steps; numerical analysis and calibration experiments. Fig. 4 shows an overview of the research methods.

This overview (Fig. 4) explicitly sees input as observable state variable(s) and output as models and optimum conditions. The intermediate computation process is a workflow of three tasks: the extraction of data and models as to the inputted state variables, the numerical analysis simplifying the extracted models with sensitivity and stability, and the calibration between data and the simplified models. Here, the system of interest is assumed to be closed and determined only by the state variables of the extracted models.

3.1. Observed SARS-CoV-2 data

The literature, knowledge bases, and databases were searched to extract actual time-series data and the models with the state variable. Here, the state variable must be an observable viral quantification in clinical tests or experiments. The viral quantification includes viral load, which one can estimate from total viral particle copies by quantitative reverse transcription-polymerase chain reaction (qRT-PCR) of the specimen such as mucus in nasopharyngeal swab collection [34].

As a case study, viral load data was used in this paper. The data was from an image of time-series data sequences of median viral load in the mild and severe patient populations (anonymized) published in the previous literature [35]. The primary source originated 96 patients with

Table 1. Summary of four viral dynamics models and their corresponding ordinary differential equations (ODEs).

Models	ODEs		
M_1: Perelson's model (baseline) [13]	dT/dt	=	$-\beta TV - \mu_1 T$
	dI/dt	=	$\beta TV - \mu_2 I$
	dV/dt	=	$-\mu_3 V + kI$
M_2: Huang's model (functional response) [21]	dT/dt	=	$-\beta TV/(1+aT+bV) - \mu_1 T$
	dI/dt	=	$\beta TV/(1+aT+bV) - \mu_2 I$
	dV/dt	=	$-\mu_3 V + kI$
M_3: Pearce-Pratt-Phillips model (viral synapse) [24]	dT/dt	=	$-\beta_1 TV - \beta_2 TI - \mu_1 T$
	dI/dt	=	$\beta_1 TV + \beta_2 TI - \mu_2 I$
	dV/dt	=	$-\mu_3 V + kI$
M_4: New model (functional response and viral synapse)	dT/dt	=	$-\beta_1 TV/(1+aT+bV) - \beta_2 TI - \mu_1 T$
	dI/dt	=	$\beta_1 TV/(1+aT+bV) + \beta_2 TI - \mu_2 I$
	dV/dt	=	$-\mu_3 V + kI$

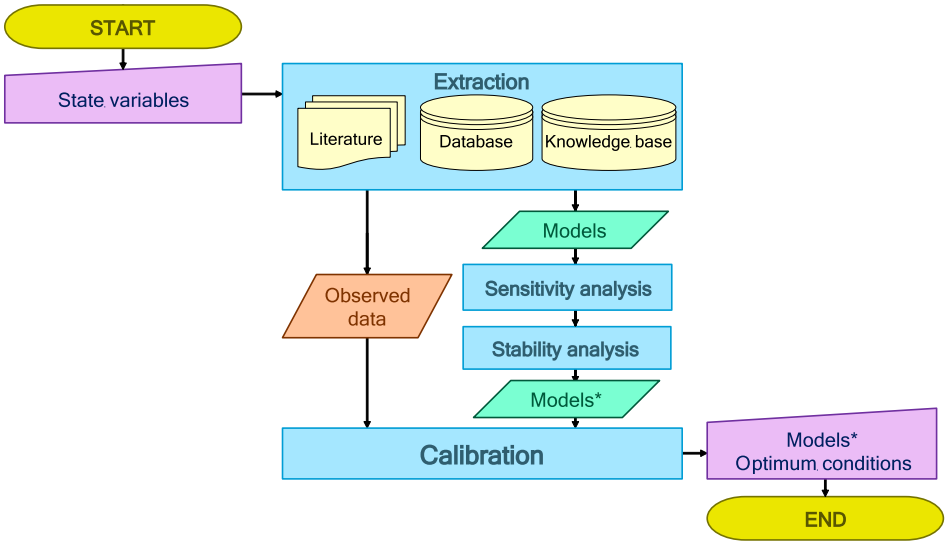

Fig. 4. Overview of research methods, explicitly seeing input as observable state variable(s) and output as models and optimum conditions.

Table 2. Summary of variables and constants and their corresponding symbols, definitions, and ranges.

Symbol	Definition	Range
t	unit time (*e.g.*, day) since symptom onset or the start of the experiment	$t \in [0\ \infty)$
T, I, V	target cell density, infectious cell density, virus density	$(T, I, V) : T \geq 0, I \geq 0, V \geq 0$
β	virus infection rate	$\beta \in (0, 1)$
k	viral shedding rate	$k \in (0, 1)$
μ_1	target cell mortality	$\mu_1 \in (0, 1)$
μ_2	infectious cell mortality	$\mu_2 \in (0, 1)$
μ_3	virus mortality	$\mu_3 \in (0, 1)$
a	proportional constant	$a \in (0, 1)$
b	proportional constant	$b \in (0, 1)$
β_1	cell-free transmission rate	$\beta_1 \in (0, 1)$
β_2	cell-to-cell transmission rate	$\beta_2 \in (0, 1)$

SARS-CoV-2 infection (22 mild patients and 74 severe patients) collected by a COVID-19 designated hospital in Zhejiang Province, China, from January 19, 2020, to March 20, 2020. This source has been licensed under the Creative Commons Attribution-NonCommercial 4.0 International (CC BY-NC 4.0) license, which has permitted to edit, process, and use it as a secondary source, subject to the author's acknowledgment [36]. The image processing via an open software *WebPlotDigitizer* version 4.3 transformed the viral load data points into coordinate values [37, 38].

Fig. 5 illustrates daily viral load sequences since symptom onset in mild and severe cases.

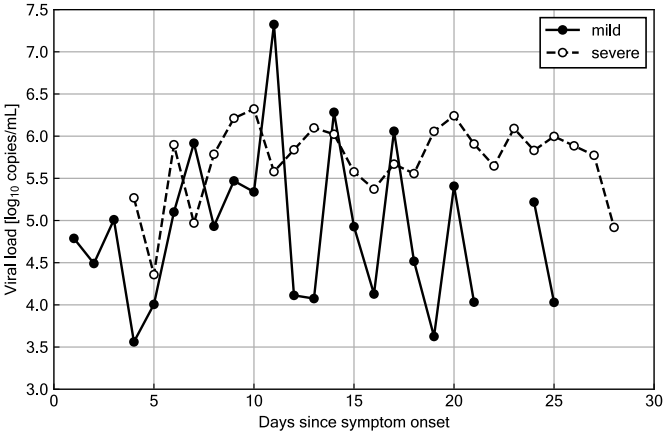

Fig. 5. Severe acute respiratory syndrome coronavirus 2 (SARS-CoV-2) viral load data across the days since symptom onset in mild cases (solid line with black markers) and severe cases (dashed line with white markers). Each of these data sequences is a derivative of original figure by Zheng *et al.*, licensed under the Creative Commons Attribution-NonCommercial 4.0 International (CC BY-NC 4.0) license.

Viral load fluctuates and attenuates in both cases over time, often higher in severe cases except on days 7, 11, 14, and 17. The missing values in the original sequences have undergone an imputation by linear interpolations.

3.2. Sensitivity analysis

Subsequently, the sensitivity analysis was devised as the model's complexity reduction process. Sensitivity analysis identifies the parameters with little effect on the output even if fixed within the boundary conditions, and thereby one is reduced to calibrating simplified models only [39, 40]. Given a nonlinear system of viral dynamics and interactivity among multiple parameters, global sensitivity analysis (GSA) was employed. Suppose d-th dimensional parameter set $(p_1, p_2, \cdots, p_d)$, where each p_i is standardized as $p_i \in [0, 1]$. i and X_i denote parameter index running over natural numbers $\{1, \ldots, d\}$ and parameter set samples with only p_i fixed respectively. The contribution of p_i to output Y variance with all parameters varied is given by:

$$S_{T_i} = 1 - \frac{\mathrm{Var}_{X_{\sim i}}(\mathrm{E}(Y \mid X_{\sim i}))}{\mathrm{Var}(Y)}$$

Where:

Var : variance
E : expected value

The Quasi-Monte Carlo sampling method generated parameter value sets (Sobol sequences) with lower discrepancy than random value sets, and thereby yielding p_i with small S_{T_i} [41, 42].

3.3. Stability analysis

Additionally, the stability analysis examined the dynamic behavior of the solution trajectory in the neighborhood of the fixed point in phase space. The purpose of stability analysis is to guarantee that any solution is stable [43]. In other words, this process can imply the necessity of other separate simulations or detailed analysis near the bifurcation parameter conditions whenever the equilibrium solution bifurcates [44]. To perform a stability analysis of stationary equilibrium solutions, one can ground the Routh-Hurwitz theorem wherein the behavior of the system near the steady-state is related to the eigenvalues of the Jacobian matrix [45, 46].

Theorem *(Routh-Hurwitz theorem). If all the eigenvalues of the Jacobian matrix have negative real parts, the stationary solution is asymptotically stable. If any eigenvalue has a positive real part, the solution is unstable; if the maximum real part of the eigenvalues equals zero, the Jacobian matrix cannot characterize the stability.*

Consequently, the eigenvalues of the Jacobian matrices of the two equilibrium solutions were calculated: the disease-free equilibrium (DFE) point, where the disease dies out, and the endemic equilibrium (EE) point, where the disease remains persistent [47]. For example, the Jacobian matrix of the M_1's DFE point $E_1 = (T_0, 0, 0)$ was

$$J(E_1) = \begin{bmatrix} -\mu_1 & 0 & -\beta T_0 \\ 0 & -\mu_2 & \beta T_0 \\ 0 & k & -\mu_3 \end{bmatrix}.$$

The Jacobian matrix of the M_1's EE point $E_1^* = (T^*, I^*, V^*)$ was

$$J(E_1^*) = \begin{bmatrix} -\mu_1 - \beta V^* & 0 & -\beta T^* \\ \beta V^* & -\mu_2 & \beta T^* \\ 0 & k & -\mu_3 \end{bmatrix}.$$

Likewise, the Jacobian matrix of the M_3's DFE point $E_3 = (T_0, 0, 0)$ was

$$J(E_3) = \begin{bmatrix} -\mu_1 & -\beta_2 T_0 & -\beta_1 T_0 \\ 0 & -\mu_2 + \beta_2 T_0 & \beta_1 T_0 \\ 0 & k & -\mu_3 \end{bmatrix}.$$

The Jacobian matrix of the M_3's EE point $E_3^* = (T^*, I^*, V^*)$ was

$$J(E_3^*) = \begin{bmatrix} -\mu_1 - \beta_1 V^* - \beta_2 I^* & -\beta_2 T^* & -\beta_1 T^* \\ \beta_1 V^* + \beta_2 I^* & -\mu_2 + \beta_2 T^* & \beta_1 T^* \\ 0 & k & -\mu_3 \end{bmatrix}.$$

The eigenvalues were calculated from these Jacobian matrices of M_1 and M_3 by SymPy 1.6.2. Finally, the artificially generated data by quadrature of the models' ODEs got calibrated to the observed data. In the calibration experiments, dynamic time warping (DTW) provided a similarity measure between the artificial time series of viral particles from the models and the actual time series of viral load [48]. Here, DTW computes the shortest path two time-series data by finding the absolute error value per point across them, which enables one to obtain the similarity even if their lengths and periods are different [49]. Global optimization of DTW distance as a cost function avoided dropping into local minima by Algorithm 1. Given that the well-posed inverse problems require that any solution is identifiable [50, 51], the calibration experiments estimated the parameter values with the finite prediction bands allowed.

Algorithm 1

Input: ODEs, Sobol sequences (n = 1000), observed data (mild or severe)
Output: estimated parameter value sets (n = 1000)

```
Param ← Sobol sequences
for int i = 1, i ≤ 50, ++i do
    initialize DataFrame (DF) to empty
    for int j = 1, j ≤ 1000, ++j do
        for int days = 0, days ≤ 200, ++days do
            SimData[j] ← ODEs integration with Param[j]
        end for
        DTWdist[j] ← DTW distance between SimData[j] and observed data
        stack (Param[j], DTWdist[j]) to DF
        sort DF (in descending order by DTWdist)
        initialize Param* to top 250 sets of Param
        for int l = 1, l ≤ 3, ++l do
            for int r = 1, r ≤ 250, ++r do
                add random float value ∈ [−0.01, 0.01] to one element of Param[r] of DF[r]
                and stack the new parameter value set to Param*
            end for
        end for
    end for
    Param ← Param*
end for
```

These methods resulted in the optimum set of models with parameter estimates. The experimental configurations were as follows: Intel(R) Core(TM) i7-7500U CPU@2.70GHz, 2904Mhz, 16GB of memory, and Microsoft(R) Windows(R) 10 Operating System.

4. Results and discussion

This section shows the results and expands the discussion.

4.1. Sensitivity analysis

As the results of GSA, the sensitivity indices with error bars are illustrated in Fig. 6.

For all models, μ had low sensitivity. a and b had almost zero sensitivities. In contrast, β and k had high sensitivities, where β became distributed between β_1 and β_2 in the models considering viral synapse. Considering that the parameters with small sensitivities can be fixable [52] and that the sensitivities for parameters other than the fixable parameters were similar, the parameter values μ_1, μ_2, μ_3, a, and b were set to zero. This parameter pruning simplified the four models into two models. In particular, M_2 was reduced into M_1 and M_4 merged into M_3. The above model simplification implied that it would be sufficient to perform stability analysis and calibration experiments only for M_1 and M_3.

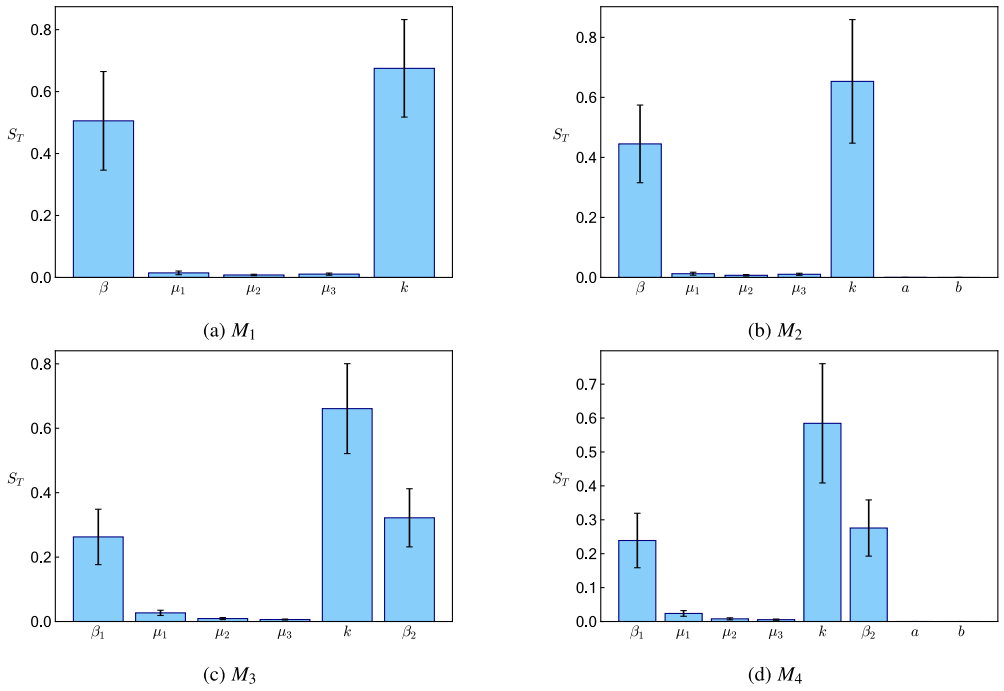

Fig. 6. Sensitivity analysis results. Each figure includes the bars reflecting sensitivities to the parameters about four models; (a) Perelson's model M_1 (b) Huang's model M_2 (c) Pearce-Pratt-Phillips model M_3 (d) original model M_4. Each error bar is a 95% confidence interval.

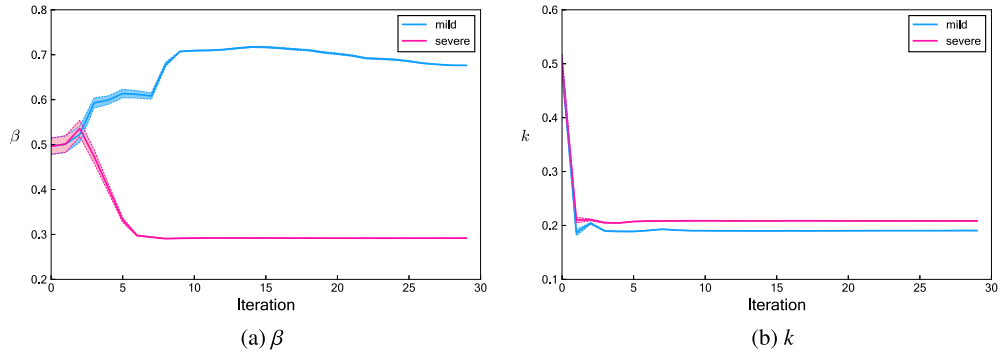

Fig. 7. Calibration results (Perelson's model M_1). The curves (blue: mild) (red: severe) are plotting the mean of estimated parameter value sets of (a) virus infection rate β (b) viral shedding rate k corresponding to the iteration number with prediction bands allowed. The dashed lines and the filled areas are the margins of errors and the prediction bands ±2SE (standard error of the mean), respectively.

4.2. Stability analysis

Next, according to the stability analysis results, all the eigenvalues of $J(E_0)$, $J(E_0^*)$, $J(E_3)$, and $J(E_3^*)$ had negative real parts. These eigenvalues guaranteed the solution's orbital stability based on the Routh-Hurwitz theorem. Namely, it could be postulated that the two equilibrium solutions, DFE point and EE point, would remain asymptotically stable, which meant no requirement of specific constraints on parameter conditions in the calibration experiments. However, it would be curious that there existed no chaos or bifurcation, and the models' stability did not correspond to the fluctuation in the observed data sequences. Therefore, further searching experimental data sequences without fluctuation over a longer period would deal with this inconsistency.

Hereinafter, the calibration results of M_1 and M_3 are shown. Fig. 7 shows the calibration results of M_1.

The horizontal and vertical axes correspond to the iteration number and the estimated parameter value sets. The blue curve stands for mild cases and the red one for severe cases. The solid lines are not regression curves but the plots of the mean of estimated values. The dashed lines are margins of errors, and the filled areas are prediction bands ±2SE (standard error of the mean). The narrower prediction band reflects the higher prediction accuracy of the mean parameter value. Considering β converged to $(0.70, 0.30)$, whereas k to $(0.19, 0.21)$ for mild and severe cases, M_1 would be an identifiable model. If the relationship between the COVID-19 severity and infection rate were not subject to other factors, it could be speculated that smaller β would have reproduced severe cases. As for k, there was little difference in the estimates between mild and severe as for viral shedding, making it difficult to give a biologically meaningful interpretation.

Fig. 8 shows the calibration results of M_3.

β_1 converged to $(0.32, 0.42)$, β_2 to $(0.25, 0.0050)$, and k to $(0.195, 0.200)$ for mild and severe cases. Regarding viral shedding term k, the same discussion as above for the M_1 results holds. The calibration experiments could not determine the true values of β_1 and β_2 accompanied with the prediction bands. Although M_3 is more complicated than M_1, M_3 would be a partially identifiable model. This difference in the prediction bands would reflect that the model complexity could be a trade-off with the identifiability in the simple model. As for the comparison between β_1 and β_2, β_2 was eightieth of β_1 in severe cases. Suppose it is true that the smaller β in Fig. 7a results in the more severe COVID-

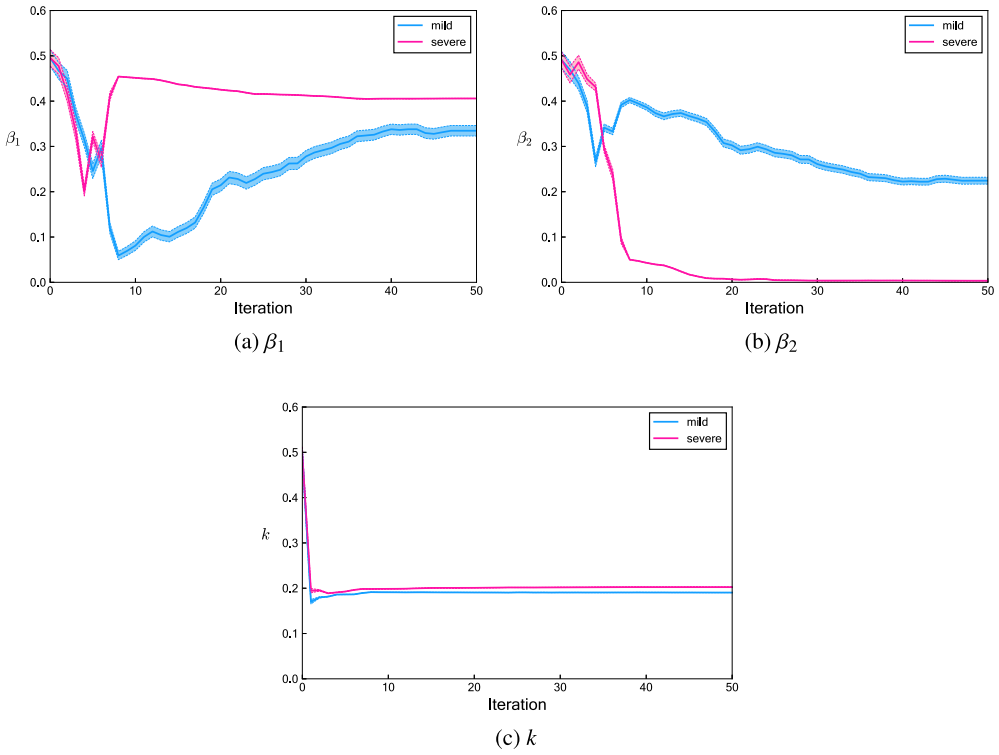

Fig. 8. Calibration results (Pearce-Pratt-Phillips model M_3). The curves (blue: mild) (red: severe) are plotting the mean of estimated parameter value sets of (a) cell-free transmission rate β_1 (b) cell-to-cell transmission rate β_2 (c) viral shedding rate k corresponding to the iteration number with prediction bands allowed. The dashed lines and the filled areas are the margins of errors and the prediction bands ±2SE (standard error of the mean), respectively.

Table 3. Summary of models and their corresponding converged values of estimated parameters. The values of (β, k) in Perelson's model M_1 and (β_1, β_2, k) in Pearce-Pratt-Phillips model M_3 are shown in mild cases and severe cases.

Model	Parameter	Mild	Severe	Description
M_1	β	0.70	0.30	virus infection rate
	k	0.19	0.21	viral shedding rate
M_3	β_1	0.32	0.42	cell-free transmission rate
	β_2	0.25	0.0050	cell-to-cell transmission rate
	k	0.195	0.200	viral shedding rate

19 symptoms. Then, β_2, which is smaller in severe cases in Fig. 8b, would be related to the severity rather than β_1. In other words, the cell-to-cell transmission would be essential for severe COVID-19 than cell-free transmission. The recent papers have reported the correlation between the COVID-19 severity and the expression level of the specific genes related to the cell-to-cell transmission on other viruses [53]. Therefore, one ideal interpretation from the calibration results would be the correlation between the cell-to-cell transmission and the COVID-19 severity. If accurate, it would lead to claiming the efficacy of drug intervention for β_2 such as a cell-to-cell transmission blocking. However, it has been still unclear whether the genes are involved in the cell-to-cell transmission in COVID-19. Hence, it is necessary to carefully validate the relationship between the cell-to-cell transmission and the COVID-19 severity. Table 3 shows the summary of the above calibration results.

5. Related work

This section compares the models in this paper with other model extensions in terms of two types of computational modeling: Agent-based modeling (ABM) and Equation-based modeling (EBM) [54]. These two modeling approaches differ in heterogeneity and homogeneity, social behavior, and schematic representation [55]. ABM is characterized by heterogeneity, *i.e.*, different characteristics at the individual level; state, location coordinates in space, age, gender, speed, degree of interaction [56]. Each individual is assumed to be a social, intelligent agent that constantly modifies its own behavioral rules through feedbacks called micro-macro loops [57, 58]. There have existed studies that employed ABM to describe the interaction of the immune system between tuberculosis and cancer [59]. In contrast, EBM is not subject to heterogeneity but relatively homogeneous, *i.e.*, the stratification is more straightforward than that of ABM, and the individual characteristics differ depending on the categorized units such as age groups, rather than on the personal level [60]. EBM often assumes neither social individual nor behavioral change; every individual is habituated as an identical particle [61]. Indeed, assuming that viruses and cells lack sociality would be reasonable. Accordingly, EBM represents a sum of individual state transitions as a stock-flow diagram or a compartment model. The choice of which modeling approach, ABM or EBM, has required consistency with the modeling goals, such as immunization policymaking [62]. This paper has opted for EBM in place of ABM for two reasons: first, the homogeneous group of cells and viral particles; second, the difficulty in procuring the spatial information required for ABM. The model extensions on EBM include the models taking into account the discrete nature of the molecules and temporal changes in the host immune response, rather than assuming a uniform probability of infection. If the number of molecules in the reaction volume is sufficiently large, the continuous ODEs, including stochastic or discrete stochastic models as more appropriate models, are sometimes helpful [63]. Compared with the asymptotically stable models, fractional models with a non-integer order derivative can reproduce more complex behavior [64]. For ex-

ample, the fractional model in the Caputo-Fabrizio derivative with a nonsingular kernel has successfully described the dynamics of hepatitis B virus or tuberculosis [65, 66]. Otherwise, the fractional model in the Atangana-Baleanu derivative with nonsingular and nonlocal kernels for the crossover behavior in the model has described the complexity of dynamics [67].

6. Conclusion

This paper investigated the different SARS-CoV-2 dynamics models with numerical analysis based on ODEs. GSA simplified the models, and stability analysis revealed that the models satisfied the stability criterion. The subsequent calibration experiments fitted the models to the observed viral load data across two types of hospitalized COVID-19 patients. The comparison of optimum parameter conditions in mild cases and severe cases indicated that cell-to-cell transmission would significantly correlate to the COVID-19 severity. As a limitation, the fidelity and sample size of data were not appropriate to negate the inconsistency with the experimental data fluctuation. These limitations made the arguments only from the interpretations in this paper unsound. To surmount these limitations, fetching fine-grained SARS-CoV-2 data in a longer duration would be desirable. Otherwise, systematic review and metasynthesis on the open data platform [68] could also ensure the integrated data with higher fidelity. Given the above, further investigation would include the validation of the relationship between the cell-to-cell transmission and the COVID-19 severity and the identification of the essential factors in severe cases. Overall, future work remained, including data integration and the above relationship's validation. Still, the experiments for modeling and simulation in this paper would have contributed to exploring the plausible SARS-CoV-2 dynamics models based on numerical analysis and differential equations.

Declarations

Author contribution statement

Mitsuhiro Odaka: Conceived and designed the experiments; Performed the experiments; Analyzed and interpreted the data; Contributed reagents, materials, analysis tools or data; Wrote the paper.

Katsumi Inoue: Conceived and designed the experiments; Analyzed and interpreted the data; Contributed reagents, materials, analysis tools or data.

Funding statement

Katsumi Inoue was supported by the Japan Society for the Promotion of Science (JSPS KAKENHI Grant Number JP17H00763). Katsumi Inoue was supported by the Research Organization of Information and Systems.

Data availability statement

Data included in article/supplementary material/referenced in article.

Declaration of interests statement

The authors declare no conflict of interest.

Additional information

No additional information is available for this paper.

Acknowledgements

The authors express gratitude to Professor Morgan Magnin for suggesting the topic treated in this paper.

References

[1] P. Zhou, X.L. Yang, X.G. Wang, et al., A pneumonia outbreak associated with a new coronavirus of probable bat origin, Nature 579 (7798) (2020) 270–273.
[2] A. Remuzzi, G. Remuzzi, COVID-19 and Italy: what next?, Lancet 395 (2020) 1225–1228.
[3] E. Dong, H. Du, L. Gardner, An interactive web-based dashboard to track COVID-19 in real time, Lancet Infect. Dis. 20 (5) (2020) 533–534.
[4] D.L. Smith, K.E. Battle, S.I. Hay, et al., Ross, Macdonald, and a theory for the dynamics and control of mosquito-transmitted pathogens, PLoS Pathog. 8 (4) (2012) 1–13.
[5] W.H. Hamer, The Milroy lectures on epidemic disease in England—the evidence of variability and persistence of type, Lancet 167 (4305) (1906) 569–574.
[6] R. Ross, Some quantitative studies in epidemiology, Nature 87 (2188) (1911) 466–467.
[7] W.O. Kermack, A.G. McKendrick, G.T. Walker, A contribution to the mathematical theory of epidemics, Proc. R. Soc. A 115 (772) (1927) 700–721.
[8] W.O. Kermack, A.G. McKendrick, Contributions to the mathematical theory of epidemics. III.—Further studies of the problem of endemicity, Proc. R. Soc. A 141 (843) (1933) 94–122.
[9] G. Giordano, F. Blanchini, R. Bruno, et al., Modelling the COVID-19 epidemic and implementation of population-wide interventions in Italy, Nat. Med. 26 (2020) 1–6.
[10] S. He, Y. Peng, K. Sun, SEIR modeling of the COVID-19 and its dynamics, Nonlinear Dyn. 101 (3) (2020) 1667–1680.
[11] A. Murray, G. Jackson, Viral dynamics: a model of the effects of size shape, motion and abundance of single-celled planktonic organisms and other particles, Mar. Ecol. Prog. Ser. 89 (1992) 103–116.
[12] F. Barré-Sinoussi, J.C. Chermann, F. Rey, et al., Isolation of a T-lymphotropic retrovirus from a patient at risk for acquired immune deficiency syndrome (AIDS), Science 220 (4599) (1983) 868–871.
[13] A.S. Perelson, A.U. Neumann, M. Markowitz, et al., HIV-1 dynamics in vivo: virion clearance rate, infected cell life-span, and viral generation time, Science 271 (5255) (1996) 1582–1586.
[14] M.A. Nowak, C.R. Bangham, Population dynamics of immune responses to persistent viruses, Science 272 (5258) (1996) 74–79.
[15] A.S. Perelson, Modelling viral and immune system dynamics, Nat. Rev. Immunol. 2 (1) (2002) 28–36.
[16] M. Torres, J. Wang, P.J. Yannie, et al., Identifying important parameters in the inflammatory process with a mathematical model of immune cell influx and macrophage polarization, PLoS Comput. Biol. 15 (2019) 1–27.
[17] M. Postel, A. Karam, G. Pézeron, et al., A multiscale mathematical model of cell dynamics during neurogenesis in the mouse cerebral cortex, BMC Bioinform. 20 (470) (2019).
[18] T. Guo, Z. Qiu, K. Kitagawa, et al., Modeling HIV multiple infection, J. Theor. Biol. 509 (2021) 110502.
[19] A. Neumann, N. Lam, H. Dahari, et al., Hepatitis C viral dynamics in vivo and the antiviral efficacy of interferon-α therapy, Science 282 (1998) 103–107.
[20] M. Odaka, K. Inoue, Computational modeling and simulation of viral load kinetics in SARS-CoV-2 replication, in: CSBio'20: Proceedings of the Eleventh International Conference on Computational Systems-Biology and Bioinformatics, 2020, pp. 75–82.
[21] G. Huang, W. Ma, Y. Takeuchi, Global properties for virus dynamics model with Beddington-DeAngelis functional response, Appl. Math. Lett. 22 (11) (2009) 1690–1693.
[22] J.R. Beddington, Mutual interference between parasites or predators and its effect on searching efficiency, J. Anim. Ecol. 44 (1) (1975) 331–340.
[23] D.L. DeAngelis, R.A. Goldstein, R.V. O'Neill, A model for tropic interaction, Ecology 56 (4) (1975) 881–892.
[24] R. Pearce-Pratt, D. Malamud, D.M. Phillips, Role of the cytoskeleton in cell-to-cell transmission of human immunodeficiency virus, J. Virol. 68 (5) (1994) 2898–2905.
[25] T. Igakura, J.C. Stinchcombe, P.K.C. Goon, et al., Spread of HTLV-I between lymphocytes by virus-induced polarization of the cytoskeleton, Science 299 (5613) (2003) 1713–1716.
[26] W. Weissenhorn, A. Dessen, L.J. Calder, et al., Structural basis for membrane fusion by enveloped viruses, Mol. Membr. Biol. 16 (1) (1999) 3–9.
[27] A.C. Walls, Y. Park, M.A. Tortorici, et al., Structure, function, and antigenicity of the SARS-CoV-2 spike glycoprotein, Cell 181 (2) (2020) 281–292.e6.
[28] M. Hoffmann, H. Kleine-Weber, S. Simon, et al., SARS-CoV-2 cell entry depends on ACE2 and TMPRSS2 and is blocked by a clinically proven protease inhibitor, Cell 181 (2020) 271–280.e8.
[29] P. V'kovski, A. Kratzel, S. Steiner, et al., Coronavirus biology and replication: implications for SARS-CoV-2, Nat. Rev. Microbiol. 19 (3) (2021) 155–170.
[30] K.S. Jones, C. Petrow-Sadowski, Y.K. Huang, et al., Cell-free HTLV-1 infects dendritic cells leading to transmission and transformation of CD4+ T cells, Nat. Med. 14 (2008) 429–436.
[31] A. Pais-Correia, M. Sachse, S. Guadagnini, et al., Biofilm-like extracellular viral assemblies mediate HTLV-1 cell-to-cell transmission at virological synapses, Nat. Med. 16 (2010) 83–89.
[32] J.R. Koza, Human-competitive results produced by genetic programming, Genet. Program. Evol. Mach. 11 (3–4) (2010) 251–284.

[33] J. Page, R. Poli, W.B. Langdon, Smooth Uniform Crossover with Smooth Point Mutation in Genetic Programming: A Preliminary Study, in: European Conference on Genetic Programming, Springer, 1999, pp. 39–48.
[34] X. He, E.H.Y. Lau, P. Wu, et al., Author correction: temporal dynamics in viral shedding and transmissibility of COVID-19, Nat. Med. 26 (2020) 1491–1493.
[35] S. Zheng, J. Fan, F. Yu, et al., Viral load dynamics and disease severity in patients infected with SARS-CoV-2 in Zhejiang province, China, January-March 2020: retrospective cohort study, BMJ 369 (2020) m1443.
[36] Creative Commons Attribution-NonCommercial 4.0 International, https://creativecommons.org/licenses/by-nc/4.0/. (Accessed 4 September 2021).
[37] D. Drevon, S.R. Fursa, A.L. Malcolm, Intercoder reliability and validity of WebPlotDigitizer in extracting graphed data, Behav. Modif. 41 (2) (2017) 323–339.
[38] A. Rohatgi, Webplotdigitizer: Version 4.3, https://automeris.io/WebPlotDigitizer, 2020. (Accessed 4 September 2021).
[39] E. Kent, S. Neumann, U. Kummer, et al., What can we learn from global sensitivity analysis of biochemical systems?, PLoS ONE 8 (11) (2013) 1–13.
[40] B. Anderson, E. Borgonovo, M. Galeotti, et al., Uncertainty in climate change modeling: can global sensitivity analysis be of help?, Risk Anal. 34 (2014) 271–293.
[41] I.M. Sobol, Global sensitivity indices for nonlinear mathematical models and their Monte Carlo estimates, Math. Comput. Simul. 55 (1–3) (2001) 271–280.
[42] A. Saltelli, Making best use of model evaluations to compute sensitivity indices, Comput. Phys. Commun. 145 (2) (2002) 280–297.
[43] Y.A. Kuznetsov, Elements of Applied Bifurcation Theory, Springer-Verlag, 1998.
[44] L. Dai, D. Vorselen, K.S. Korolev, et al., Generic indicators for loss of resilience before a tipping point leading to population collapse, Science 336 (2012) 1175–1177.
[45] E.J. Routh, A Treatise on the Stability of a Given State of Motion, Particularly Steady Motion, Macmillan and Company, 1877.
[46] A. Hurwitz, Ueber die Bedingungen, unter welchen eine Gleichung nur Wurzeln mit negativen reellen Theilen besitzt, Math. Ann. 46 (1895) 273–284.
[47] R. Sun, Global stability of the endemic equilibrium of multigroup SIR models with nonlinear incidence, Comput. Math. Appl. 60 (2010) 2286–2291.
[48] D.J. Berndt, J. Clifford, Using dynamic time warping to find patterns in time series, in: Proceedings of the 3rd International Conference on Knowledge Discovery and Data Mining, AAAI Press, 1994, pp. 359–370.
[49] F. Petitjean, A. Ketterlin, P. Gançarski, A global averaging method for dynamic time warping, with applications to clustering, Pattern Recognit. 44 (2011) 678–693.
[50] A. Tarantola, Popper, Bayes and the inverse problem, Nat. Phys. 2 (2006) 492–494.
[51] G. Yu, G. Sapiro, S. Mallat, Solving inverse problems with piecewise linear estimators: from Gaussian mixture models to structured sparsity, IEEE Trans. Image Process. 21 (2012) 2481–2499.
[52] A. Saltelli, P. Annoni, I. Azzini, et al., Variance based sensitivity analysis of model output. Design and estimator for the total sensitivity index, Comput. Phys. Commun. 181 (2) (2010) 259–270.
[53] M. Tong, Y. Jiang, D. Xia, et al., Elevated expression of serum endothelial cell adhesion molecules in COVID-19 patients, J. Infect. Dis. 222 (6) (2020) 894–898.
[54] H.V.D. Parunak, R. Savit, R.L. Riolo, Agent-based modeling vs. equation-based modeling: a case study and users' guide, in: Multi-Agent Systems and Agent-Based Simulation, Springer, Berlin Heidelberg, 1998, pp. 10–25.
[55] M. Holcombe, X-machines as a basis for dynamic system specification, Softw. Eng. J. 3 (1988) 69–76.
[56] Y. Vodovotz, G. An, Agent-based models of inflammation in translational systems biology: a decade later, Wiley Interdiscip. Rev., Syst. Biol. Med. 11 (6) (2019) e1460.
[57] G. Andrighetto, R. Conte, P. Turrini, et al., Emergence in the loop: simulating the two way dynamics of norm innovation, in: Normative Multi-Agent Systems, 2007, http://drops.dagstuhl.de/opus/volltexte/2007/907.
[58] T.N.A. Nguyen, J.-D. Zucker, D.H. Nguyen, et al., A hybrid macro-micro pedestrians evacuation model to speed up simulation in road networks, in: Advanced Agent Technology, AAMAS'11, 2011, pp. 371–383.
[59] S.B. Shinde, M.P. Kurhekar, Review of the systems biology of the immune system using agent-based models, IET Syst. Biol. 12 (3) (2018) 83–92.
[60] G. Bobashev, D. Goedecke, F. Yu, et al., A hybrid epidemic model: combining the advantages of agent-based and equation-based approaches, in: Proceedings of the Winter Simulation Conference, WSC 2007, 2007, pp. 1532–1537.
[61] R. Mach, F. Schweitzer, Modeling vortex swarming in Daphnia, Bull. Math. Biol. 69 (2007) 539–562.
[62] R.M. Anderson, B.T. Grenfell, Quantitative investigations of different vaccination policies for the control of congenital rubella syndrome (CRS) in the United Kingdom, Epidemiol. Infect. 96 (2) (1986) 305–333.
[63] Y. Yuan, L.J.S. Allen, Stochastic models for virus and immune system dynamics, Math. Biosci. 234 (2) (2011) 84–94.
[64] M.A. Khan, A. Atangana, Modeling the dynamics of novel coronavirus (2019-nCov) with fractional derivative, Alex. Eng. J. 59 (4) (2020) 2379–2389.
[65] S. Ullah, M.A. Khan, M. Farooq, A new fractional model for the dynamics of the hepatitis B virus using the Caputo-Fabrizio derivative, Eur. Phys. J. Plus 133 (6) (2018) 1–14.
[66] S. Ullah, M.A. Khan, M. Farooq, A fractional model for the dynamics of TB virus, Chaos Solitons Fractals 116 (2018) 63–71.
[67] M.A. Khan, S. Ullah, M. Farooq, A new fractional model for tuberculosis with relapse via Atangana-Baleanu derivative, Chaos Solitons Fractals 116 (2018) 227–238.
[68] G.M. Bwire, M.V. Majigo, B.J. Njiro, et al., Detection profile of SARS-CoV-2 using RT-PCR in different types of clinical specimens: a systematic review and meta-analysis, J. Med. Virol. 93 (2) (2021) 719–725.